Title

An energy-based analysis framework for soil structure interaction systems

Authors

Yang, Han
Wang, Hexiang
Jeremić, Boris

Publication Date

2022-06-01

DOI

10.1016/j.compstruc.2022.106758

Peer reviewed

An Energy-Based Analysis Framework for Soil Structure Interaction Systems

Han Yang[a], Hexiang Wang[a], Boris Jeremić[a,*]

[a]*Department of Civil and Environmental Engineering, University of California, Davis, CA, USA*

Abstract

Presented is an energy-based analysis and design framework for soil structure interaction system. Theoretical formulation based on thermodynamics and engineering mechanics for calculating energy dissipation in soil and structural elastic plastic finite elements is presented and discussed. The importance of incorporation of plastic free energy, that ensures nonnegative incremental energy dissipation, also known as the second law of thermodynamics, is emphasized. For application to practical engineering problems, the presented framework is implemented in the Real-ESSI Simulator and visualized using ParaView. In order to illustrate the proposed framework, a practical model composed of a reinforced concrete frame structure, underlying soil, and soil-foundation interface is developed and analyzed. Elastic-plastic material model and viscous, Rayleigh damping parameters are calibrated to represent typical realistic cases. Spatial and time distribution of energy dissipation density is analyzed and discussed. Locations with high plastic energy dissipation, used as a proxy for material and structural damage are identified. In addition, locations of high plastic energy dissipation within soil and soil-foundation interface, that are used to dissipate seismic energy before it reaches structure, are also identified. Influences of input seismic motion scale and design variation on system performance are investigated. It is shown that traditional displacement-based design parameters, such as peak displacement and maximum interstory drift ratio, could underestimate the change of system performance when different seismic motion scale or structural design are used.

1. Introduction

The use of energy dissipation, as well as other energy-based parameters, is gaining popularity in design of structures and soil structure interaction (SSI) systems. As pointed out by Papazafeiropoulos et al. [36], the traditional force-based and displacement-based design concepts only focus on the peak responses of a structural system, while the loading history is usually not taken into account. During an extreme loading event, such as an earthquake, structures are exited by a number of cycles of loadings and are

*Corresponding authors
Email address: jeremic@ucdavis.edu (Boris Jeremić)

continuously damaged throughout the loading history. Unlike force or displacement, that generally fluctuate during cyclic loading, energy dissipation continuously accumulates with a nonnegative rate as material is being damaged. Energy dissipation is, therefore, more suitable to be used as an effective design parameter in seismic design of soil structure systems.

When the concept of energy-based design (EBD) was first proposed, the available computational power for engineering design was rather limited. Energy analysis methods were developed for single degree of freedom (SDOF) and multiple degree of freedom (MDOF) systems [59, 60, 50, 30, 45, 49]. The simplification of realistic soil structure systems to SDOF or MDOF systems has been widely used in the field of civil engineering, and carried out in more recent studies related to EBD [31, 10, 34, 33, 36]. Noted EBD approaches have been fairly successful, and many were adopted in actual designs and design codes.

With the development of modern computers and modern computational programs, it is now feasible to model components and complete SSI systems with much higher fidelity models. High fidelity numerical modeling and simulation tools, such as the Real-ESSI Simulator [25] used in this study, are capable of modeling the nonlinear, inelastic behavior of complete earthquake soil structure interacting (ESSI) systems. Material models and finite elements for different components of an ESSI system, with various levels of sophistication, have been developed and widely used [27, 32, 40, 18, 58, 44]. Using modern, available modeling and simulation techniques, modern EBD can be improved to a new level of accuracy and efficiency.

Figure 1 illustrates processes and mechanisms of the propagation and dissipation of seismic energy, from earthquake source to location of the soil structure system. Upon reaching the site, only part of the mechanical energy carried by the seismic waves flows through the local SSI system, and leads to the dynamic responses of soil and structure. Another part of the input mechanical energy is reflected back and propagates outside of the local domain of interest. This phenomenon is usually referred to as radiation damping. Obviously, the mechanical energy is not transformed into other energy forms, and no change of entropy happens during this process. Therefore, the energy loss due to radiation damping is considered separately from other physical energy dissipation mechanisms.

Within the local SSI system, seismic energy is dissipated due to material inelasticity in soil, structure, and foundation-soil interface zone, viscous coupling between soil grains and pore fluids, and energy dissipators placed in the building or foundation. In addition to the physical dissipative processes, algorithmic damping [4] is frequently used to achieve stable simulation result in numerical studies. As pointed out by Yang et al. [57], these energy dissipation mechanisms model fundamentally different physical or mathematical phenomena, and do lead to different system responses. It is important to model each energy dissipation mechanism by following proper physics and mathematics.

Material inelasticity leads to plastic energy dissipation, also known as hysteretic energy or hysteretic energy dissipation. Plastic energy dissipation is directly related to material damage, and thus often used to evaluate design safety. Correct modeling of plastic energy dissipation requires consideration of plastic free energy, which is related to the internal structure, or fabric, of inelastic material. Early work published by Farren and Taylor [16] and Taylor and Quinney [47] identified the role of plastic free energy and

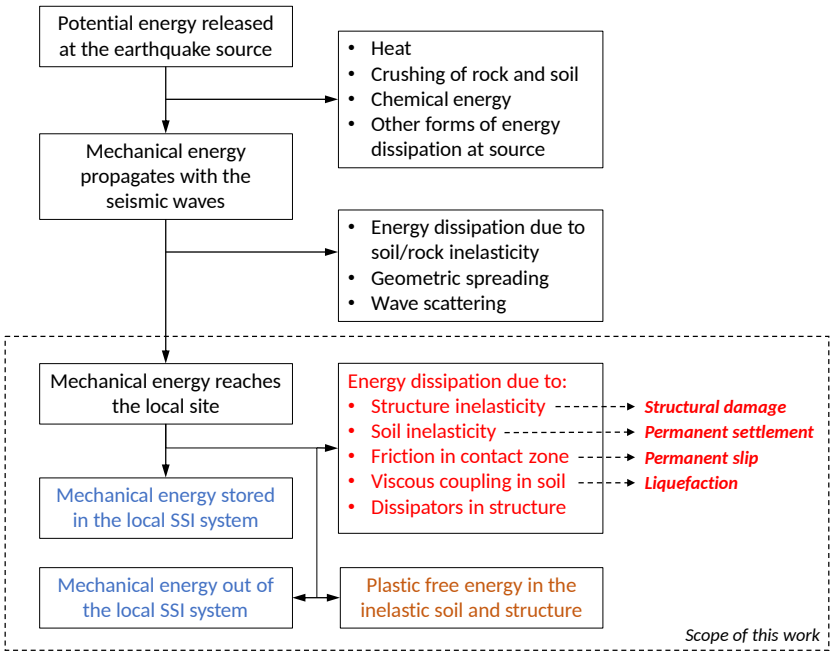

Fig. 1. Seismic energy propagation and dissipation, from source to local site.

plastic energy dissipation in material deformation and damage. More theoretical and experimental studies on this topic include those by Ziegler and Wehrli [61], Collins and Houlsby [15], Rittel [37], Rosakis et al. [38], Feigenbaum and Dafalias [17], Veveakis et al. [51], Yang et al. [54], and Yang et al. [56].

When modeling a realistic SSI system, each component should be modeled with a appropriate material model (sand, clay, rock, steel, concrete, isolator, damper, or other soil and structural material) that was developed using proper theoretical framework and assumptions. Many of the traditional, still popular soil models simply neglect plastic free energy. This neglect leads to a common misconception about plastic work and plastic energy dissipation. Collins and Kelly [14] analyzed a family of soil models, including Mohr-Coulomb, original Cam Clay, modified Cam Clay, using the thermo-mechanical theory. Feigenbaum and Dafalias [17] presented a new interpretation of the pressure-independent, von Mises type material models under the thermomechanical framework. Yang et al. [56] proposed an energy dissipation computation approach for the pressure-dependent, Drucker-Prager plasticity models.

For the modeling of structural component, for example beam-column elements and wall elements, nonlinear fiber section technique developed by Spacone et al. [44] has been widely used. A number of fiber material models were developed to be used together with fiber section. The uniaxial steel model originally developed by Menegotto and Pinto [32] and later extended by Filippou et al. [18] is capable of capturing the nonlinear hysteretic behavior and isotropic strain-hardening effect of steel. Some popular choices for uniaxial concrete models include those developed by Kent and Park [27], Scott et al.

[40], and Yassin [58]. The formulations of plastic energy dissipation for the previously mentioned models were presented by Yang et al. [55].

The second energy dissipation mechanism, viscous damping, is the result of dissipative interactions between solids and viscous fluids in a SSI system. In order to obtain reliable simulation results, both natural viscous damping, caused by structure vibration through the air or water, and artificial viscous damping, from viscous damper and dissipator, need to be properly modeled. Caughey damping [11], as well as its special case, Rayleigh damping, is usually used to model viscous damping. As pointed out by Hall [20], Rayleigh damping can cause unrealistically high damping forces, if the damping parameters are not chosen properly.

The last energy dissipation mechanism, numerical, algorithmic damping, does not represent any physical process, however it is used in time integration algorithms to achieve stable, converging simulation results. Newmark family algorithms [35, 23, 13] are the most commonly used time integration schemes. Traditionally, these algorithms were considered to conserve the total mechanical energy of simulated system for some combination of the integration parameters, for example by choosing $\gamma = 0.500$ and $\beta = 0.250$ for Newmark algorithm. Krenk [28] found that the Newmark algorithms could lose their energy conserving properties for geometric nonlinear problems, contact problems, and large time step simulations. A few energy conserving time integration algorithms [41, 8, 19, 28]) have been developed to address this issue. Nonetheless, the Newmark algorithm is still a popular choice and has proven to be reliable for finite element (FE) simulations.

The theoretical and computational basis for each energy dissipation mechanism was laid out in a series of publications [54, 57, 55, 56]. As a next step, presented here is a modernized EBD framework that incorporates previously developed methods. Using this framework, the energy dissipation due to different dissipative mechanisms are continuously computed throughout the simulation. More importantly, the distribution of energy dissipation density in space in time, within the model can be analyzed and used to identify zones with large viscous damping or significant material damage. These results can be directly used in the evaluation and optimization of engineering designs.

The following section summarizes the formulations for energy dissipation due to material inelasticity, Rayleigh damping, and algorithmic damping. Next, a SSI system consisting of a 4-story 4-bay frame structure, underlying soil, and the interface zone between footing and soil is modeled and analyzed. The energy dissipation results of the model under various loading conditions are presented and discussed, in order to illustrate the application of the proposed EBD framework.

2. Energy Computation Framework

Significant amount of potential energy is released at the earthquake source, fault when the earthquake initiates [3]. Mechanical energy from this release propagates as seismic waves. During the wave propagation process, majority of the released energy is dissipated, due to various mechanisms, and also spreads to the earth's crust. Only a small percentage of the released seismic energy reaches the local site of interest on or close to the surface. As shown in Figure 1, the presented framework focuses

on modeling the transformation and dissipation of seismic energy that reaches an SSI system on or close to the ground surface.

The incremental form of energy balance for a dynamic inelastic system can be expressed as

$$\Delta E_I = \Delta E_K + \Delta D_V + \Delta W_M \tag{1}$$

where the right hand side of Equation 1 is the increment of input energy ΔE_I, and the three terms on the left hand side of Equation 1 are the increment of kinetic energy ΔE_K, the increment of viscous energy dissipation ΔD_V, and the increment of material work of the system ΔW_M. Equation 1 can be derived from the general equation of motion for dynamic inelastic systems, as was shown by Yang et al. [57].

It is noted that all equations in this work are presented in their incremental form. This is because the proposed equations are implemented in a FE modeling and simulation platform, Real-ESSI Simulator [25], that is based on time-domain, incremental analysis.

The incremental material work ΔW_M component can be further decomposed into specific energy terms that are related to different energy dissipation behavior of inelastic materials:

$$\Delta W_M = \Delta E_S + \Delta E_P + \Delta D_P \tag{2}$$

where ΔE_S is the incremental elastic strain energy, ΔE_P is the incremental plastic free energy, and ΔD_P is the incremental plastic energy dissipation.

Computation of plastic free energy and plastic energy dissipation for various inelastic material models is challenging. This is due to to the fact that many commonly used material models were developed based on force-displacement or stress-strain responses, without much consideration of energy dissipation behavior. The following section presents a series of energy computation formulation for inelastic solid, beam-column element, and contact/interface material models. The computation of viscous energy dissipation and the effects of numerical damping are also discussed. Some of the equations and derivations presented below were developed in full detail in previous studies [54, 57, 55, 56].

2.1. Plastic Energy Dissipation

Incremental material work equation 2 can be rewritten in a local form, that yields the equation for plastic energy dissipation density:

$$\Phi = \sigma_{ij}\Delta\epsilon_{ij} - \sigma_{ij}\Delta\epsilon_{ij}^{el} - \Delta\Psi^{pl} = \sigma_{ij}\Delta\epsilon_{ij}^{pl} - \Delta\Psi^{pl} \geq 0 \tag{3}$$

where Φ is the incremental plastic energy dissipation density, σ_{ij} is the stress tensor, $\Delta\epsilon_{ij}$ is the incremental strain tensor, $\Delta\epsilon_{ij}^{el}$ is the incremental elastic strain tensor, $\Delta\epsilon_{ij}^{pl}$ is the incremental plastic strain tensor, and $\Delta\Psi^{pl}$ is the incremental plastic free energy density. It is worth pointing out that, according to the second law of thermodynamics, the incremental plastic energy dissipation density should always be nonnegative during any time period. The violations of this law were observed in a large number of published papers, and continues to emerge in more recent publications.

For material models developed based on the classic small deformation elastoplasticity theory, the stress σ_{ij}, total strain ϵ_{ij}, elastic strain ϵ_{ij}^{el}, and plastic strain ϵ_{ij}^{pl} are

readily defined. These tensors can be directly obtained from constitutive level algorithms and used in energy computations during numerical simulations. On the other hand, the plastic free energy density Ψ^{pl} was not defined for many inelastic material models when they were developed. Since each model features specific assumptions, the computation of plastic free energy and plastic energy dissipation must be tailored for the each corresponding model. In what follows, presented is the theoretical formulation of plastic free energy and plastic energy dissipation for different types of material models that are frequently used in a practical SSI analysis.

2.1.1. Von Mises Plasticity for Pressure-Independent Solid

Von Mises elastic-plastic model is one of the simplest yet effective constitutive models for pressure-independent materials. It is commonly used in a SSI models for metal components as well as for total stress analysis of saturated soil. The yield function of von Mises plasticity is expressed as

$$f = \sqrt{(s_{ij} - \alpha_{ij})(s_{ij} - \alpha_{ij})} - \sqrt{\frac{2}{3}}k \tag{4}$$

where $s_{ij} = \sigma_{ij} - (1/3)\sigma_{kk}$ is the deviatoric part of the stress tensor, α_{ij} is the back stress tensor defined as the center of yield surface in stress space, and k is the size of yield surface in stress space. The variables α_{ij} and k are known as the internal variables in classic plasticity theory.

To model the cyclic nonlinear post-yield behavior, von Mises plasticity is often used together with Armstrong-Frederick kinematic hardening [5]. The nonlinear evolution of the back stress tensor α_{ij} is defined incrementally as

$$\Delta\alpha_{ij} = \left[\frac{2}{3}h_a m_{ij} - c_r \alpha_{ij}\sqrt{\frac{2}{3}m_{rs}m_{rs}}\right]\Delta\lambda \tag{5}$$

where m_{ij} is the normalized plastic flow direction tensor, $\Delta\lambda$ is the scalar loading index that equals to the magnitude of incremental plastic strain, and h_a and c_r are the nonnegative hardening constants.

For von Mises plasticity model with Armstrong-Frederick kinematic hardening, the incremental plastic free energy density is written as

$$\Delta\Psi^{pl} = \frac{3}{2h_a}\alpha_{ij}\Delta\alpha_{ij} \tag{6}$$

Detailed derivation and discussion on Equation 6 were presented earlier by Yang et al. [54]. Plastic energy dissipation can then be calculated by substituting Equation 6 into Equation 3.

2.1.2. Drucker-Prager Plasticity for Pressure-Dependent Solid

Drucker-Prager type plasticity is used to model pressure-dependent materials, for example soil, in an SSI system. It was shown by Yang et al. [56] that Drucker-Prager plasticity with associated plastic flow rule is thermodynamically inappropriate as the incremental plastic work, defined as $\sigma_{ij}\Delta\epsilon_{ij}^{pl}$, is always zero. In addition, Collins and

Houlsby [15] pointed out that non-associated plastic flow rule appears naturally for a pressure-dependent frictional material. Thus, the Drucker-Prager plasticity referred to in this paper is non-associated, that is, the plastic flow direction is not normal to the yield surface in stress space.

The general form of Drucker-Prager yield function is

$$f = \sqrt{(s_{ij} - p\alpha_{ij})(s_{ij} - p\alpha_{ij})} - \sqrt{\frac{2}{3}}kp \tag{7}$$

where $p = -(1/3)\sigma_{kk}$ is the mean stress, or hydrostatic pressure, applied on the material. Note that in Drucker-Prager plasticity, the internal variables k and α_{ij} are dimensionless, while they have the dimension of stress in von Mises plasticity.

Armstrong-Frederick nonlinear kinematic hardening is considered again, in a slightly different form, to accommodate Drucker-Prager plasticity:

$$\Delta\alpha_{ij} = \left(\frac{2}{3}h_a m_{ij}^{dev} - c_r\alpha_{ij}\sqrt{\frac{2}{3}m_{rs}^{dev}m_{rs}^{dev}}\right)\Delta\lambda \tag{8}$$

where m_{ij}^{dev} is the deviatoric part of the normalized plastic flow direction tensor m_{ij}.

For non-associated Drucker-Prager plasticity model with Armstrong-Frederick kinematic hardening, the incremental plastic free energy density is written as

$$\Delta\Psi^{pl} = \left(\frac{3}{2h_a}\alpha_{ij}\Delta\alpha_{ij} - m_{ii}^{vol}\Delta\lambda\right)p \tag{9}$$

where m_{ij}^{vol} is the volumetric part of the normalized plastic flow direction tensor m_{ij}. Note that the main differences between Equation 9, for Drucker-Prager plasticity, and Equation 6, for von Mises plasticity, are the pressure dependency and an additional term for volumetric plastic flow. Details on Equation 9 were discussed in detail by Yang et al. [56]. After plastic free energy is obtained, the plastic energy dissipation is calculated by substituting Equation 9 into Equation 3.

2.1.3. Steel Fiber Material for Beam-Column

For moment frame structures, beam-column elements are usually used for modeling and simulation. Fiber section method developed by Spacone et al. [43] is one of the most popular and effective approaches to model the nonlinear/inelastic behavior of beam-columns. Uniaxial fiber materials are used to represent the concrete and/or steel rebars on a section. It is noted that fiber section method makes an assumption that only normal stress is present within a section. In other words, fiber section method is strictly applicable for pure bending and normal force loads, neglecting any influence of shear forces. However, fiber method is regularly applied to frame structural model, and it does perform well, particularly for slender beam-column elements, where influence of shear forces and shear deformation is not significant.

The energy computation approach for uniaxial steel and concrete fibers developed by Yang et al. [55] is used in this study. Key aspects of this approach are summarized in this section. Note that all the variables, including stresses and strains, in this section, are

scalars as the fiber material model is uniaxial, hence it represents relationship between uniaxial stress and uniaxial strain.

The uniaxial steel model used in this study was developed by Menegotto and Pinto [32] and extended by Filippou et al. [18]. As shown in Figure 2, this model is capable of capturing the nonlinear hysteretic behavior and isotropic strain-hardening of steel. The constitutive behavior of the steel fiber is defined as

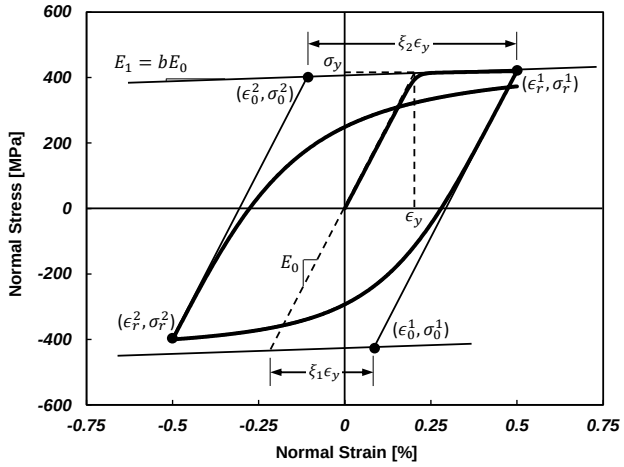

Fig. 2. Constitutive model of the uniaxial steel fiber material.

$$\sigma^* = b\epsilon^* + \frac{(1-b)\epsilon^*}{(1+\epsilon^{*R})^{1/R}} \tag{10}$$

with

$$\epsilon^* = \frac{\epsilon - \epsilon_r}{\epsilon_0 - \epsilon_r}; \quad \sigma^* = \frac{\sigma - \sigma_r}{\sigma_0 - \sigma_r} \tag{11}$$

where parameter b is the strain-hardening ratio, ϵ_r and σ_r are the strain and stress at the point of strain reversal, ϵ_0 and σ_0 are the strain and stress at the point of intersection of the two asymptotes, and parameter R is the curvature parameter that governs the shape of the transition curve between the two asymptotes.

According to Yang et al. [56], the incremental plastic free energy density is defined as

$$\Delta\Psi^{pl} = \frac{1}{2}\left[(\sigma + \sigma_r)\,\Delta\epsilon + \left(\epsilon_{pl} - \epsilon_r\right)\Delta\sigma\right] \tag{12}$$

where ϵ_{pl} is the plastic strain defined as $\epsilon_{pl} = \epsilon - \sigma/E_0$. The incremental plastic dissipation density is then obtained as

$$\Phi = \frac{1}{2}[(\sigma - \sigma_r)\Delta\epsilon - (\epsilon - \epsilon_r)\Delta\sigma] \tag{13}$$

It is important to point out that Equations 12 and 13 ensures that the incremental plastic dissipation is nonnegative, satisfying the second law of thermodynamics.

2.1.4. Concrete Fiber Material for Beam-Column

Concrete and steel fibers are used to model a reinforced concrete beam-column section. The concrete material model used in this study was proposed by Yassin [58]. As shown in Figure 3, this model is capable of modeling the cyclic hysteretic behavior and damage effects in concrete. It is noted that the full formulation of this model is somewhat convoluted, especially when considering cyclic behavior. Thus only equations that are pivotal for energy computation are shown here.

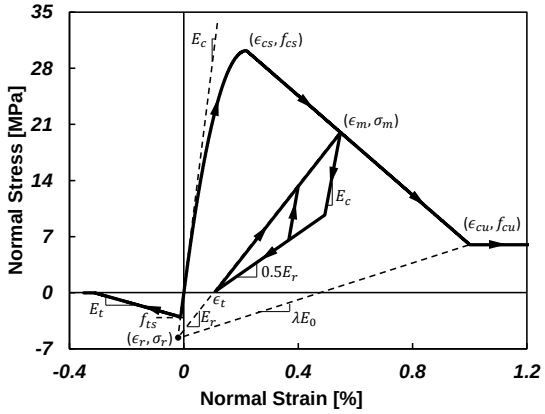

Fig. 3. Constitutive model of the uniaxial concrete fiber material.

The compressive envelope curve of this model is based on the work of Kent and Park [27] and Scott et al. [40]. The monotonic compressive behavior of the model is defined as

$$\text{If} \quad 0 \le \epsilon_m \le \epsilon_{cs} : \qquad \sigma_m = f_{cs}\left[2\left(\frac{\epsilon_m}{\epsilon_{cs}}\right) - \left(\frac{\epsilon_m}{\epsilon_{cs}}\right)^2\right] \tag{14}$$

$$\text{If} \quad \epsilon_{cs} < \epsilon_m \le \epsilon_{cu} : \qquad \sigma_m = \frac{\epsilon_m - \epsilon_{cs}}{\epsilon_{cu} - \epsilon_{cs}}(f_{cu} - f_{cs}) + f_{cs} \tag{15}$$

$$\text{If} \quad \epsilon_m > \epsilon_{cu} : \qquad \sigma_m = f_{cu} \tag{16}$$

where ϵ_m is the maximum compressive strain of the material in its loading history, σ_m is the maximum compressive stress in loading history, f_{cs} is the maximum compressive strength, ϵ_{cs} is the concrete strain at compressive strength, f_{cu} is the ultimate (crushing) strength of the concrete material, ϵ_{cu} is the concrete strain at ultimate strength, and E_{in} is the initial concrete tangent stiffness that can be calculated from $E_{in} = 2f_{cs}/\epsilon_{cs}$. The loading history variables ϵ_m and σ_m serve as internal variables in this model. Note that the material constants f_{cs}, ϵ_{cs}, f_{cu}, and ϵ_{cu} are provided by the users, and should be determined from experiments.

The cyclic behavior of the model is tied to a stress state where all reloading paths

intersect. The stress and strain at this reloading intersection are given as

$$\epsilon_r = \frac{f_{cu} - \lambda E_{in}\epsilon_{cu}}{E_{in}(1-\lambda)} \tag{17}$$

$$\sigma_r = E_{in}\epsilon_r \tag{18}$$

where λ is another material constant that is related to the ultimate strength f_{cu} and crushing strain ϵ_{cu} of the concrete. As shown in Figure 3, the unloading path consists of two linear sections that depend on the current strain ϵ and current stress σ, as well as the internal variables ϵ_m and σ_m. From the functions that define the two sections, the stress and strain at the slope change location on the unloading path is calculated from the following equations:

$$\epsilon_k = \frac{\sigma + 0.5E_r\epsilon_t - E_{in}\epsilon}{0.5E_r - E_{in}} \tag{19}$$

$$\sigma_k = 0.5E_r(\epsilon_k - \epsilon_t) \tag{20}$$

where

$$E_r = \frac{\sigma_m - \sigma_r}{\epsilon_m - \epsilon_r} \tag{21}$$

$$\epsilon_t = \epsilon_m - \frac{\sigma_m}{E_r} \tag{22}$$

The computation of energy dissipation follows two assumptions that are consistent with experimental observations on concrete material:

- Plastic energy dissipation is significant during initial monotonic loading, especially if the applied strain exceeds the material strength.
- Plastic energy dissipation also happens during subsequent cyclic loading, only if the stress reaches an upper bound of cyclic stress during reloading [55].

The incremental plastic free energy density is calculated from

$$\Delta\Psi^{pl} = \frac{1}{2}\left[\sigma_k(\Delta\epsilon_{pl} - \Delta\epsilon_t) + \Delta\sigma_k(\epsilon_{pl} - \epsilon_t)\right] \tag{23}$$

The incremental plastic energy dissipation is then

$$\Phi = \sigma\Delta\epsilon_{pl} + \frac{1}{2}\left[\sigma_k(\Delta\epsilon_t - \Delta\epsilon_{pl}) + \Delta\sigma_k(\epsilon_t - \epsilon_{pl})\right] \tag{24}$$

where the plastic strain ϵ_{pl} is defined as $\epsilon_{pl} = \epsilon - \sigma/E_{in}$. Note that Equations 23 and 24 are simplified forms of the corresponding equations provided by Yang et al. [55].

2.1.5. Soil-Foundation Interface Material

The soil-foundation interface is a thin layer of soil that is adjacent to the foundation. The contact/interface bears large normal and shear stresses and exhibits different constitutive behavior than the soil that is further away from the foundation. Significant seismic energy often dissipates within the interface zone before reaching the structure. It is therefor necessary to include the modeling of energy dissipation for soil-structure interface zone within the energy analysis framework.

The interface material model used in this study was developed by Sinha and Jeremić [42]. The stress-based interface model is capable of modeling the normal, axial nonlinear response when the gap is closed. Normal, axial response also allows for gap to open, through material nonlinear response. It is important to note that gap opening is modeled using material nonlinear response, essentially material loosing stiffness when gap opens. Shear, tangential behavior is modeled using frictional slip, with a a number of different material models controlling such inelastic shear behavior. The 3D version of the material model features one normal, axial direction that is perpendicular to the interface surface and two shear directions that are orthogonal to the normal direction.

As note above, the normal behavior is nonlinear elastic with no tensile capacity. The normal stress σ_n and normal stiffness k_n are defined as

$$\sigma_n = k_i e^{-S_r \epsilon} \epsilon \tag{25}$$

$$k_n = k_i e^{-S_r \epsilon} (1 - S_r \epsilon) \tag{26}$$

where k_i is the initial normal stiffness between soil-structure interface, S_r is the stiffening rate, and ϵ is the penetration or normal strain. Note that a maximum normal stiffness k_n^{max} is applied as a limiting case in order to avoid numerical instability.

The shear component of the interface model follows the elastoplastic theory. In order to make the interface shear behavior pressure-dependent, the elastic shear stiffness k_t is related to the normal stress σ_n. For a given normal stress σ_n, the shear stiffness k_t is defined as

$$k_t = k_{t0} \frac{\sigma_n}{\sigma_{p0}} \tag{27}$$

where σ_{p0} is the constant reference stress of 101.3kPa and k_{t0} is the shear stiffness at the reference normal stress. The yielding, slipping condition is determined by the following yield function

$$f = \left(\frac{\tau_1}{\sigma_n} - \alpha_1 \right)^2 + \left(\frac{\tau_2}{\sigma_n} - \alpha_2 \right)^2 = 0 \tag{28}$$

where τ_1 and τ_2 are the shear stress components and α_1 and α_2 are the corresponding back stress components. The evolution of back stress is of a nonlinear Armstrong-Frederick hardening type that is given as

$$\Delta\alpha_1 = k_t \Delta\gamma_1^p - \frac{k_t}{\mu_r} |\Delta\gamma^p| \alpha_1 \tag{29}$$

$$\Delta\alpha_2 = k_t \Delta\gamma_2^p - \frac{k_t}{\mu_r} |\Delta\gamma^p| \alpha_2 \tag{30}$$

where γ_1^p, γ_2^p are the plastic parts of the shear strains, μ_r is the residual, or peak normalized shear stress, and $|\Delta\gamma^p|$ is the magnitude of the incremental plastic strain defined as $|\Delta\gamma^p| = \sqrt{\Delta\gamma_1^p \Delta\gamma_2^p}$.

The energy calculation for the interface material was presented by Sinha and Jeremić [42] based on the work by Yang et al. [54]. Since the normal behavior of the material

model is nonlinear elastic, the plastic energy dissipation results from the frictional slipping in the shear directions. The incremental plastic free energy density is given as

$$\Delta\Psi^{pl} = \frac{1}{k_t}(\alpha_1\Delta\alpha_1 + \alpha_2\Delta\alpha_2) \tag{31}$$

The incremental plastic energy dissipation is then calculated from

$$\Phi = (\tau_1\Delta\gamma_1^p + \tau_2\Delta\gamma_2^p) - \Delta\Psi^{pl} \tag{32}$$

2.2. Viscous Damping

Besides plastic energy dissipation, viscous damping is another physical form of energy dissipation within an SSI system. In current practice, viscous damping is commonly modeled using Rayleigh damping, due to its simplicity and effectiveness. The incremental energy dissipation caused by viscous damping ΔD_V, from Equation 1, can be calculated using the equation given by Yang et al. [57]

$$\Delta D_V = C_{ij}\dot{u}_j\Delta u_i \tag{33}$$

where C_{ij} is the damping matrix and u_i is the generalized displacement vector. A damping matrix of the Rayleigh type can be written as

$$C_{ij} = a_M M_{ij} + a_K K_{ij} \tag{34}$$

where a_M and a_K are the damping coefficients, M_{ij} is the mass matrix, and K_{ij} is the stiffness matrix. Note that the stiffness matrix used to construct the damping matrix is usually the initial tangent stiffness matrix. Since the mass matrix and initial stiffness matrix in finite element analysis are both constant, Equation 34 indicates that the damping matrix C_{ij} is constant through the entire simulation.

When proper values of parameters are used, Rayleigh damping can provide controlled velocity proportional damping for a prescribed frequency range [4]. Hall [20] presented the equation used to compute the damping constants

$$a_M = \frac{4\xi\hat{\omega}R}{1 + R + 2\sqrt{R}} \tag{35}$$

$$a_K = \frac{4\xi}{\hat{\omega}(1 + R + 2\sqrt{R})} \tag{36}$$

where ξ is the desired damping ratio, while $\hat{\omega}$ and $R\hat{\omega}$ define the prescribed frequency range. As pointed out by Hall [20], the damping ratios can be unrealistically high for the eigen-modes outside the prescribed frequency range. It is thus noted that Rayleigh damping should always be used with damping coefficients that are calculated for appropriate damping ratio and frequency range.

2.3. Numerical Damping

For time domain FE simulations, numerical, algorithmic damping is almost always present Due to system discretization, both in space and time, spurious high frequency

motions are introduced into FE models and continue to grow as the simulation advances [4, 24]. The purpose of numerical damping is to damp out these unrealistic high frequency motions, so that the actual system response can be accurately captured.

It is important to realize that a high level of numerical damping reduces system response at all frequencies. Unrealistically high levels of numerical damping have been seen in quite a number of publications and presentations, if this information was even provided. For nonlinear inelastic systems, numerical damping helps to achieve stable and converged simulation results. However, numerical simulation results with inappropriate numerical damping are not reliable, and could lead to incorrect results, thus affecting conclusions.

From the perspective of energy analysis, numerical damping reduces the total mechanical energy in the simulated system. This is acceptable if the amount of energy loss caused by numerical damping is small enough to keep the system response unaffected. For the Newmark algorithm used in this study, numerical damping is excluded if the Newmark parameters are set to $\gamma = 0.500$ and $\beta = 0.250$ [24, 24]. Yang et al. [57] demonstrated that the amount of energy dissipation caused by numerical damping quickly increases as the Newmark parameters become larger. In one case of wave propagation in elastic-plastic media, when the Newmark parameters were set to $\gamma = 0.550$ and $\beta = 0.276$, the input energy was mostly dissipated by numerical damping, while the effects of material inelasticity and viscous damping were overshadowed. It is thus advisable to perform a sensitivity study or effects numerical damping has on a analysis results, and to keep in mind that the original purpose of numerical damping was to reduce high frequency modes introduces in the FE model by the discretization process.

3. Numerical Examples

The presented EBD analysis framework has been implemented in the Real-ESSI Simulator [25], a software, hardware and documentation system for high fidelity, high performance, time domain, linear or nonlinear/inelastic, deterministic or probabilistic, FE modeling and simulation (`http://real-essi.info`). All aforementioned material models, elements, damping types, and solution schemes that are necessary for analyzing a SSI system are available in Real-ESSI Simulator. The energy analysis results can be directly visualized using ParaView [6], with appropriate plugins, as described at `http://real-essi.info`, so that analysts can use energy dissipation information to assess their designs.

In this section, a practical SSI model composed of a moment frame structure, foundation and the underlying soils, is analyzed to illustrate the presented EBD framework. A variation of input motion intensities as well as foundation design variations are considered. Through the comparison between different cases, the effectiveness of using energy dissipation in engineering designs will be highlighted.

3.1. Modeling and Simulation Details

An overview of the SSI model is shown in Figure 4. The main components of the model are:

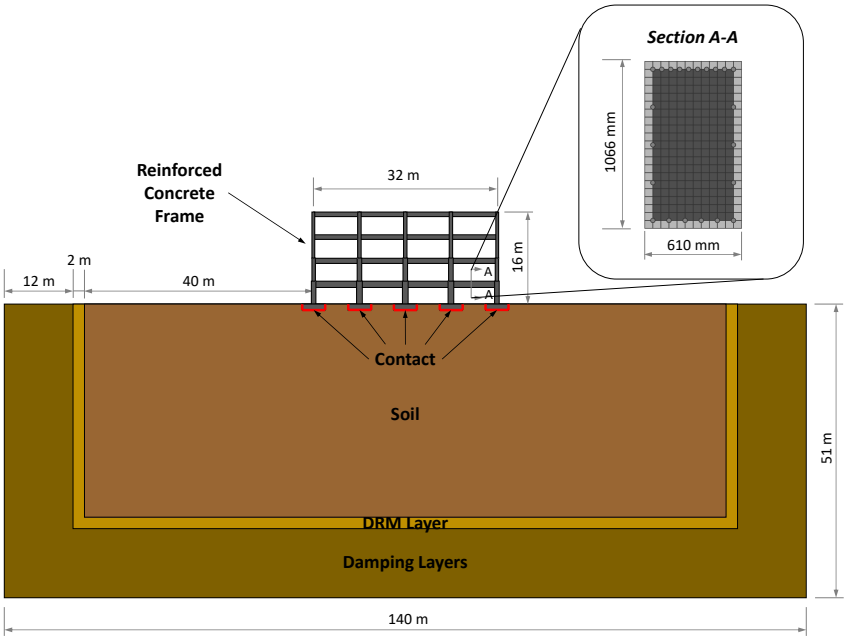

Fig. 4. Numerical model of the reinforced concrete frame, inelastic soil, and frictional interfaces.

1. A reinforced concrete frame that is modeled using beam-column elements, that are developed using previously discussed steel and concrete fiber material models. Frame model is constrained to the loading plane, it is a 2D frame model. The four story, four bay frame shown in Figure 5 is based on one of the code-conforming designs by Haselton et al. [21].

2. The underlying soil that is modeled using standard 27-node-brick elements constrained to deform in the loading plane.

3. The underlying soil is modeled using Drucker-Prager inelastic material model with Armstrong-Frederick kinematic hardening.

4. The interfaces between soil and foundation is modeled using the nonlinear, stress-based, frictional slipping contact/interface elements.

5. A layer of Domain Reduction Method (DRM) elements, for applying earthquake loading [9], is modeled using 27-node-brick elements and linear elastic material.

6. A few damping layers outside of the DRM layer, to absorb the very small outgoing waves, representing radiation damping from oscillations of the structure, are used, with progressively increasing Rayleigh damping.

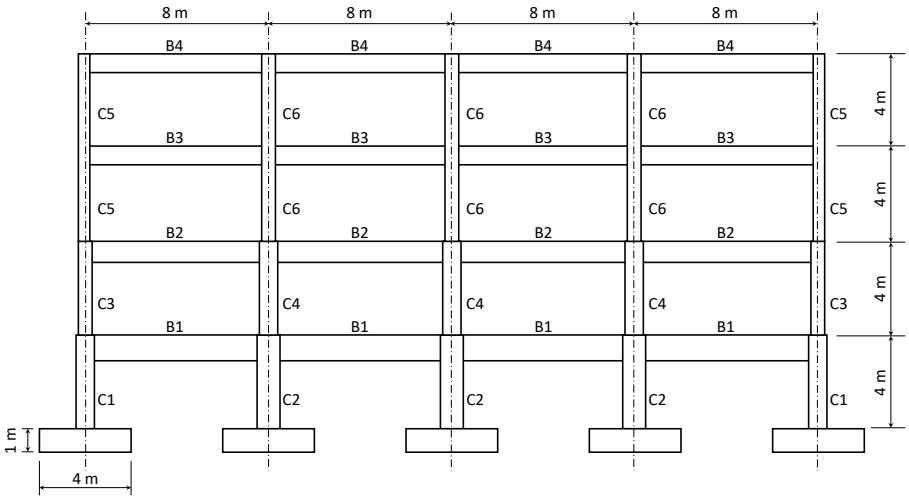

Fig. 5. Geometrical details of the reinforced concrete frame.

3.1.1. Material Parameter Calibration

The steel and concrete material parameters are calibrated using a comprehensive study by Haselton et al. [21], where both experimental and numerical results of a reinforced concrete frame building were presented. Note that Haselton et al. [21] also used fiber section technique and the same material models for steel and concrete as in this study. The parameter calibration results for the uniaxial concrete and steel materials under cyclic loading are shown in Figure 6. A satisfying match between the cyclic beam-

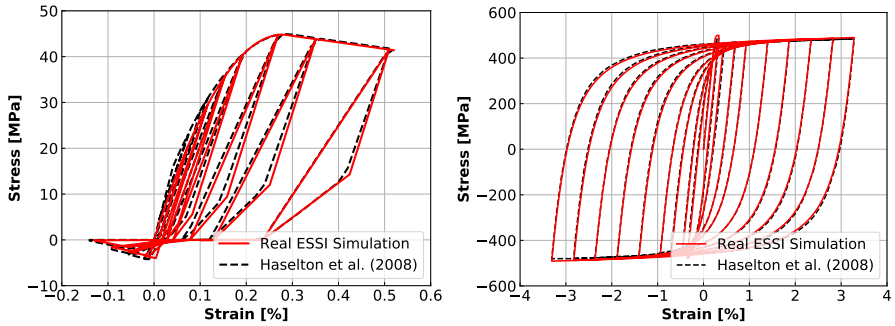

(a) Confined concrete **(b)** Steel

Fig. 6. Parameter calibration result for the uniaxial fiber materials under cyclic loading.

column section, material behavior from Real-ESSI simulation and Haselton et al. [21] are noted.

Soil beneath structural foundation was chosen to be represented by the Sacramento River sand. The experimental results of Sacramento river sand conducted by Lee and

Seed [29] have been used to calibrate and validate constitutive models in a number of studies [7, 46, 12]. In this paper, the drained triaxial test results of Sacramento river sand under confining pressures of p_0 = 290kPa, p_0 = 590kPa, and p_0 = 1030kPa are used to calibrate constitutive model parameters. Figure 7 shows the experimental and numerical drained triaxial test results on Sacramento river sand. It is observed that the volumetric

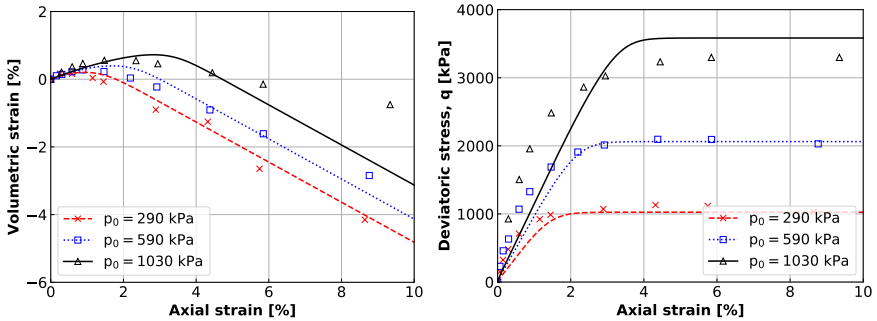

(a) **(b)**

Fig. 7. Comparison between experimental and numerical drained triaxial test results on Sacramento river sand. Experimental data after Lee and Seed [29].

strain behavior and deviatoric stress response of the numerical tests correspond well with those from the physical experiments. For the calibrated parameters, the numerical model shows good overall performance and particularly good performance for the samples under low confining pressure. When the confining pressure is relatively high, the numerical results are still acceptable, especially for small strains.

The calibrated material model parameters are summarized in Table 1.

Table 1. Material model parameters used in this study.

Steel Fiber		Concrete Fiber			Soil	
			Confined	Unconfined		
σ_y (MPa)	500	f_{cs} (MPa)	-44.82	-34.47	ρ (kg/m^3)	2000
E_0 (GPa)	200	ϵ_{cs}	-0.0028	-0.0025	E (MPa)	150
b	0.001	f_{cu} (MPa)	-8.96	0.0	ν	0.3
R	18.0	ϵ_{cu}	-0.028	-0.004	k_0	0.107
c_{R_1}	0.925	λ	0.08	0.08	h_a (MPa)	45
c_{R_2}	0.15	f_{ts} (MPa)	4.0	4.0	c_r	300
a_1, a_3	0.0	E_t (GPa)	2.0	2.0	ξ	0.7
a_2, a_4	55.0				k_d	0.9

Analysis of eigen frequencies of the reinforced concrete frame shows that the first three eigen frequencies of the frame are f_{N1} = 1.598Hz, f_{N2} = 4.984Hz, and f_{N3} = 9.426Hz. Due to stiffness reduction caused by material inelasticity/nonlinearity, these eigenfrequencies are expected to decrease if the imposed motion is large enough to cause yielding within structural components.

3.1.2. Seismic Motions

For seismic motion application, DRM proposed by Bielak et al. [9] is used in this study. DRM is probably the best method currently available and used to apply seismic motion to SSI model [26, 2]. The main advantages of DRM are the computational efficiency and versatility, in the sense that it can be used for almost any type of SSI system and motion. DRM is further combined with the analytic solution for plane waves in layered half space [48, 22] to develop the wave potential-domain reduction method [53] that is used in this study.

One of the motions used in this study is a wavelet, a so called Ormsby wavelet motion [39, 1]. Figure 8 shows the input Ormsby motion displacements at earthquake source. The peak ground displacement at source is 0.012m. The angle of inclination of

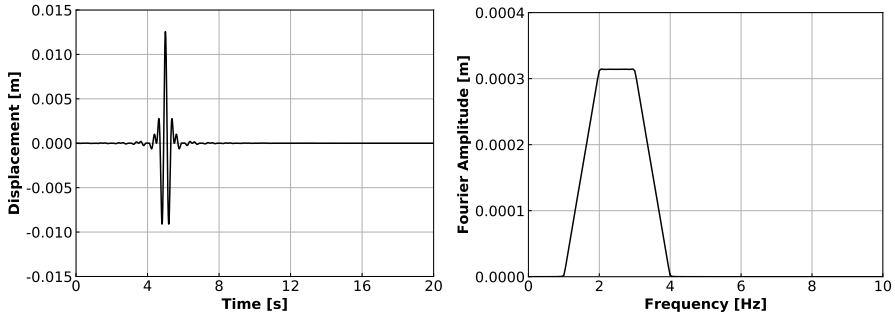

(a) Time series **(b)** FFT Spectrum

Fig. 8. Input Ormsby wavelet motion, displacements at the depth.

a plane wave propagating toward surface is 15°. The motion frequency content starts at $f_1 = 1$Hz, with a constant frequency content between $f_2 = 2$Hz and $f_3 = 3$Hz, and ends at $f_4 = 1$Hz. Figure 9 shows surface, free field acceleration resulting from applied displacement signal at the depth, that is shown in Figure 8.

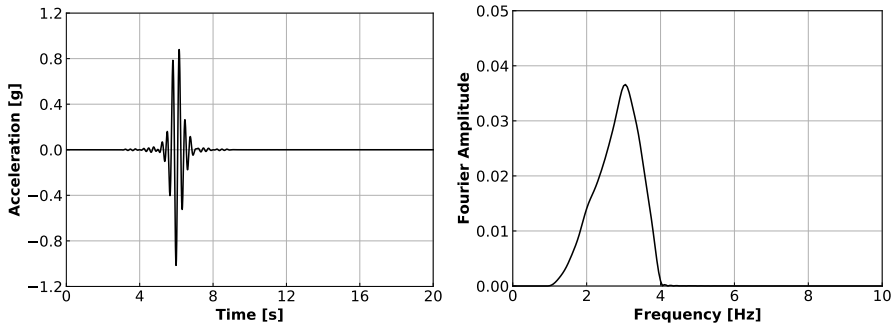

(a) Time series **(b)** FFT Spectrum

Fig. 9. Ormsby wavelet motion, surface accelerations.

3.1.3. Rayleigh Damping

Rayleigh damping is applied to the model to simulate viscous damping in the SSI system. As pointed out by Yang et al. [57], viscous damping and material inelasticity model fundamentally different physical energy dissipation mechanisms, thus should not be used interchangeably in SSI modeling. In other words, one should not use high viscous damping with linear elastic material to model nonlinear/inelastic material behavior. In this study, Rayleigh damping is used to represent the physical viscous coupling between structure/soil and fluids.

The choice of Rayleigh damping parameters depend on the natural frequency of the structure model and the frequency range of the input ground motion. According to Hall [20], it is common practice to set the lower limit of damping range according to the model's fundamental frequency. The upper damping limit is then controlled by parameter R in Equation 36, and is chosen by considering the modes that are likely to be excited by the input motion.

In this case, the fundamental frequency of the frame model is $f_{N1} = 1.598$Hz. Considering the frequency reduction due to structural system nonlinearity, the lower limit of damping frequency is set to $f_{lowN1} = 1.0$Hz. As mentioned earlier, the first two eigen-modes of the model could be excited by the input motion shown in Figure 8. Thus, the parameter R is chosen to be 5.0 so that the upper limit of damping frequency is 5.0 Hz, which is slightly larger than the second eigen-frequency of the model. Note that this set of parameters ensures that the damping ratios within the prescribed frequency range are nearly constant. This is necessary in order to avoid the unrealistic over-damping issue mentioned before.

The magnitude of Rayleigh damping is controlled by the damping ratio ξ in Equation 36. The damping ratios of frame and soil are set to 2% and 5%, respectively. Since the purpose of this numerical example is to illustrate the presented energy analysis framework, typical values of damping ratio for structure and soil are chosen.

3.2. Benchmark Case Analysis

3.2.1. Dynamic Response of the Model

Figures 10 and 11 show the horizontal displacement and acceleration responses of the top floor and bottom, foundation level of the structure. From the displacement time history, permanent deformations at the top and bottom of the frame are observed. This is expected due to structure and soil yielding and foundation-soil interface slipping. Significant structural response is observed between $t = 5$s and $t = 8$s. The peak horizontal displacement at the top is $u_{max} = 0.057$m, and the peak acceleration is $\ddot{u}_{max} \approx 1.2$g. Both peaks are recorded at time $t \approx 6$s. It is interesting to note an acceleration peak of over $\ddot{u}_{peak} = 2.5$g at the bottom of the structure, at time $t \approx 6$s. This is explained by slip and stop of the foundation-soil interface, that generates high acceleration response at that one time instance.

According to response plots in the frequency domain, two peaks, at about $f = 1$Hz and $f = 3$Hz are observed the displacement and acceleration responses at the top of frame. Considering the stiffness reduction due to structural nonlinearity, these two frequencies probably represent the first two eigenfrequencies of the yielding reinforced concrete frame ($f_{N1} = 1.60$Hz and $f_{N2} = 4.98$Hz).

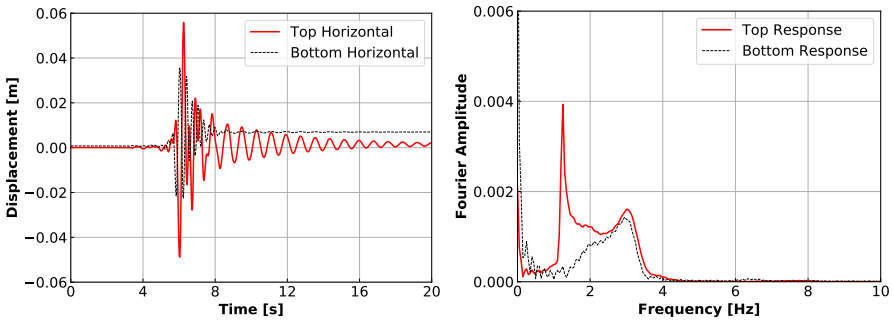

(a) Time history **(b)** FFT Spectrum

Fig. 10. Horizontal displacement response at top and bottom of the structure.

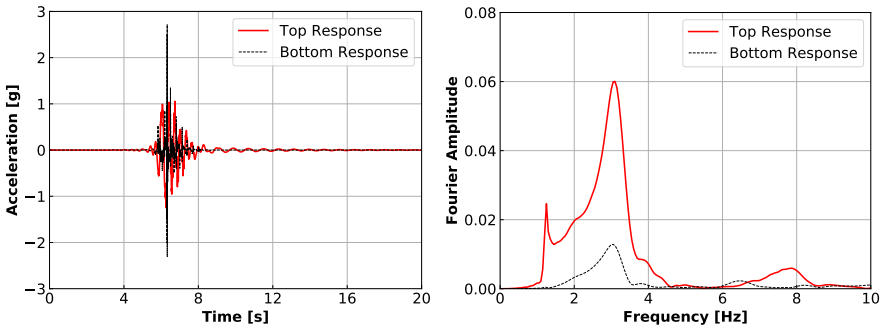

(a) Time history **(b)** FFT Spectrum

Fig. 11. Horizontal acceleration response at top and bottom of the structure.

One commonly used design parameter in structural engineering is the interstory drift ratio (IDR). Figure 12 shows the IDR time history and maximum IDR at different story levels. Peak IDR values happen at around $t = 6$s, the time when peak displacement and acceleration are recorded. Similar to displacement response, permanent IDR is observed at the end of simulation. Story 3 has the largest maximum IDR among the four floors. Maximum IDR of the frame is just over 0.8%, and that is well within design requirement.

The analysis of traditional design parameters shown above are mostly focused on the peak response of the system. However, as pointed out by Papazafeiropoulos et al. [36], the loading history and accumulated damage are also very important, perhaps even more important. As will be discussed next, energy dissipation analysis is capable of tracking continuous material yielding and damage in SSI system.

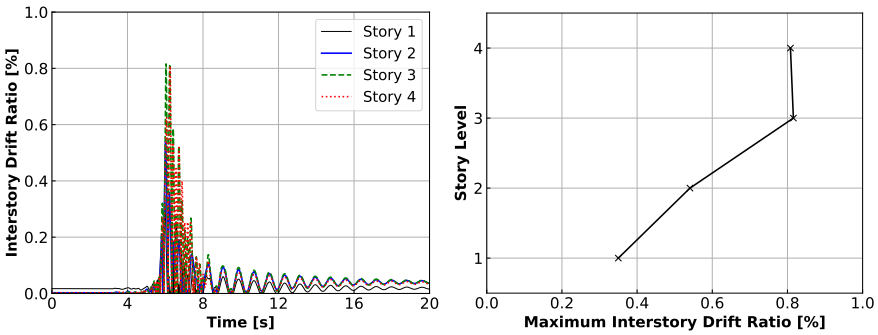

(a) Time history **(b)** Maximum values

Fig. 12. Interstory drift ratio results.

3.2.2. Energy Dissipation Analysis

Figure 13 shows the distribution of plastic energy dissipation density evolving with time. Note that for interface elements between foundation and soil, with very

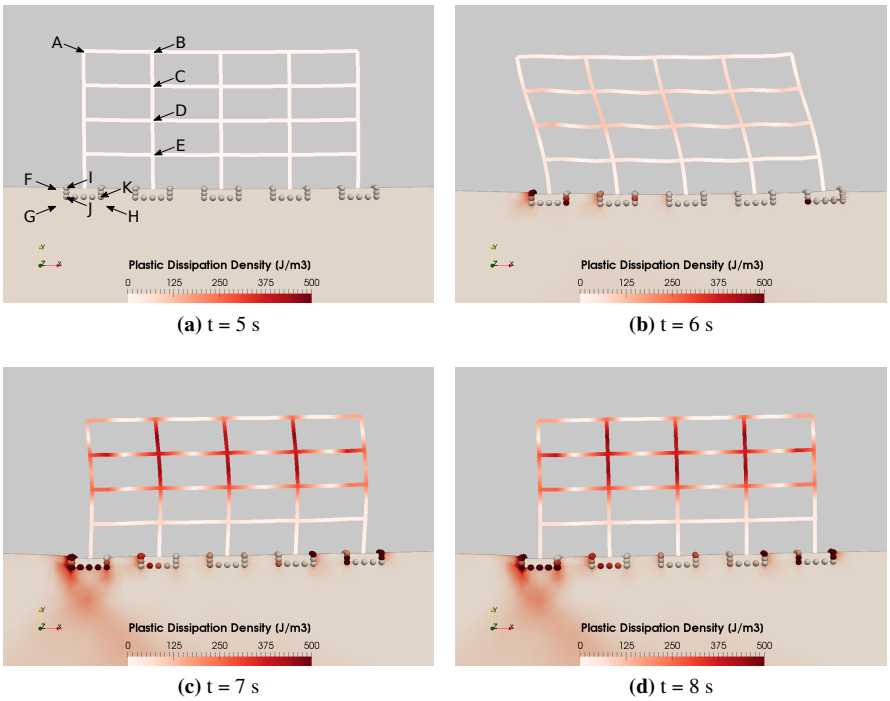

(a) t = 5 s **(b)** t = 6 s

(c) t = 7 s **(d)** t = 8 s

Fig. 13. Distribution of plastic energy dissipation density evolving with time.

small volume, small spheres are used to represent those elements in energy dissipation

visualization. At time t = 5s, as shown in Figure 13(a), before any significant seismic motion excites the frame, there is no plastic dissipation in the model. After that, between time t = 5s and time t = 8s, plastic dissipation continuously accumulates within the frame, underlying soil, and soil-structure interface zone.

Figure 13, shows that plastic dissipation in frame elements is concentrated around the connections between beams and columns. It is interesting to note that significant plastic dissipation is accumulated in the top two floors, while the lower floors experience almost no dissipation. One EBD strategy proposed by Papazafeiropoulos et al. [36] is to strive for uniform energy dissipation distribution between the floors so that the strength of all materials can be fully utilized. According to this criterion, the first-floor columns and beams are too stiff/strong compared with the structural elements at higher floors. Of course, this conclusion applies for given seismic loading, and it is possible that other seismic, or other static and/or dynamic loads might excite first floor structural elements more, thus making current design more well balanced.

Plastic dissipation in surface soil is mainly concentrated near the foundations. Large amount of plastic dissipation is observed near the left footing. This is likely due to the first significant peak of the input ground motion, and the wave traveling at an angle of 15° from left. Another interesting observation is that the damage zone in soil penetrates to some depth. This indicates not only large localized deformation around footing, but also significant settlement accumulated throughout the soil layer. Note that the settlement of the left footing is 25% larger than that of the right footing. The correlation between plastic dissipation in soil and foundation settlement shows another possible application of the proposed EBD approach.

After identifying zones with large amount of plastic dissipation, indicating structural damage and soil densification, it is interesting to investigate the accumulation of energy dissipation at specific locations. Figure 14 shows the evolution of plastic dissipation density at the locations A through K, marked in Figure 13 (a). For all locations, the rise of plastic dissipation happens at time t = 6s. This is the time when the peak displacement response is observed in Figure 10. Notice that the dissipation density at interface locations are two magnitudes larger than that at frame or soil locations. This is expected since the interface zone has much larger localized deformations, i.e. frictional slipping, that lead to highly concentrated energy dissipation. In addition, interface zone features fairly small volume, hence dissipation density is high.

Besides energy dissipation density at various locations, the total energy dissipation due to different dissipation mechanisms within soil, structure, and soil-foundation interface can also be analyzed. Figure 15 shows time histories of energy dissipation due to different mechanisms in various parts of the SSI model. Despite the high density dissipation values, as seen in Figure 14, the total plastic dissipation in contact/interface zone is smaller when compared with other energy dissipation terms. This is due to the small volume associated with the interface zone. According to Figure 15, the total energy dissipation in frame due to material inelasticity and viscous damping reach similar values at the end of simulation. For soil, on the other hand, viscous damping dissipates more energy than plasticity. It is important to note that this is due to the choices made about Rayleigh damping ratios for frame and soil. Chosen damping rations, chosen as 2% and 5% for structure and soil, respectively, were probably too high. Physically, plasticity and damage are the main energy dissipation mechanisms

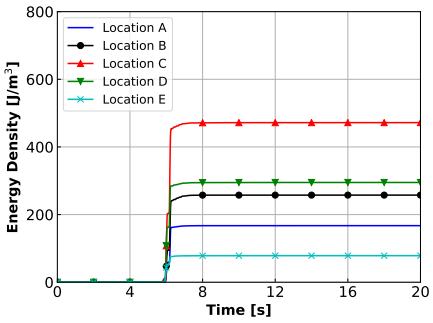

(a) Frame locations

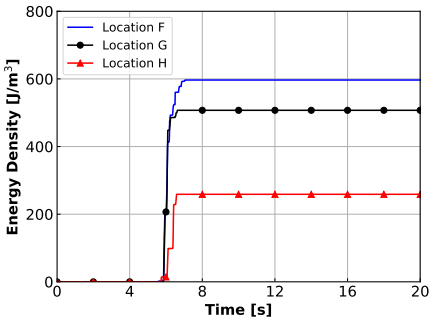

(b) Soil locations

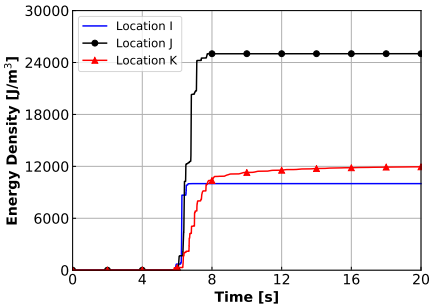

(c) Interface locations

Fig. 14. Evolution of plastic dissipation density at various locations.

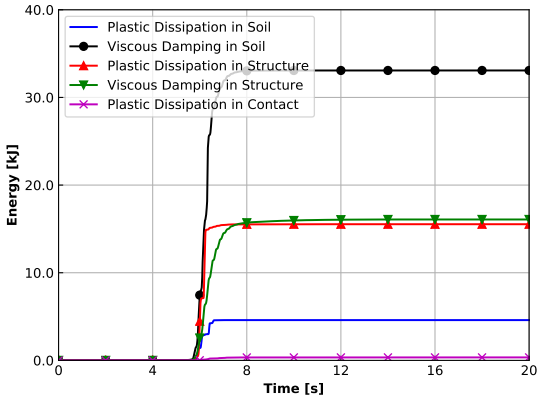

Fig. 15. Total energy dissipation due to different mechanisms in various parts of the SSI model.

for any significant seismic response of soil structure systems. Hence, for seismic motions chosen here, energy dissipation due to plasticity should be higher then energy dissipation due to viscous damping. Higher values for viscous damping, as chosen

in this example, are usually used when no inelastic deformation, and hence no plastic dissipation, is considered. Alternative results, with smaller viscous damping for soil and structure, presented next, will illustrate further illustrate this.

It should also be noted that only the soil within two meters (2m) of foundation is considered when calculating total energy dissipation in Figure 15. As indicated in Figure 13, energy dissipation also exists in soil volume at deeper depths. In fact, if the entire soil volume is considered, energy dissipation in structure and interface elements would be relatively very small, as soil will dissipate largest amount of energy due to its large volume.

3.3. Influence of Rayleigh Damping

As discussed earlier, the choice of Rayleigh damping parameters could change the dynamic response and energy dissipation of a SSI system significantly. In this section, the Rayleigh damping ratios ξ for frame and soil are reduced to 0.4% and 1%, respectively. The frequency coverage, defined by parameters R and $\hat{\omega}$, remains unchanged.

Figures 16 and 17 show the horizontal displacement and acceleration responses of top floor and foundation level of the structure.

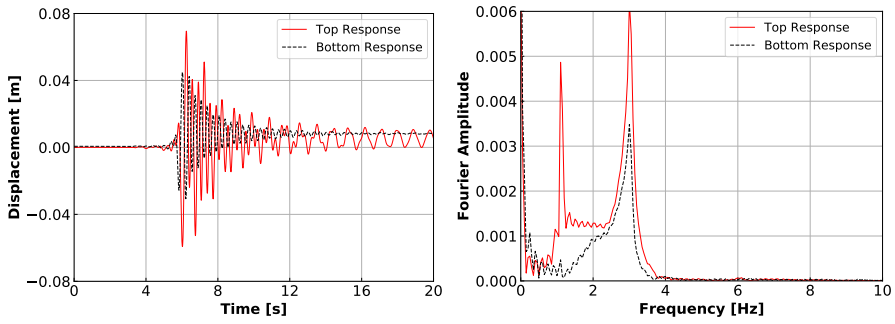

(a) Time history **(b)** FFT Spectrum

Fig. 16. Horizontal displacement response at top and bottom of the structure when Rayleigh damping ratios ξ for frame and soil are reduced to 0.4% and 1%, respectively.

Compared with Figures 10 and 11, the displacement and acceleration responses increase when Rayleigh damping ratio is decreased, as expected. This is especially notable in the FFT spectrum where the peak at 3Hz becomes much more prominent. However, the increase is not as large as it might have been expected, with a five times decrease in viscous damping. This is due to the fact that with reduced viscous damping, more realistic energy dissipation mechanics, the plastic energy dissipation in soil, interfaces and structure, dissipated much more energy, and thus balanced energy dissipation between viscous and plasticity energy dissipation.

Figure 18 shows the time histories of energy dissipation in the SSI system when Rayleigh damping ratio is reduced. The amounts of energy dissipation due to plasticity in soil, structure, and interface elements all increase considerably, as noted previously.

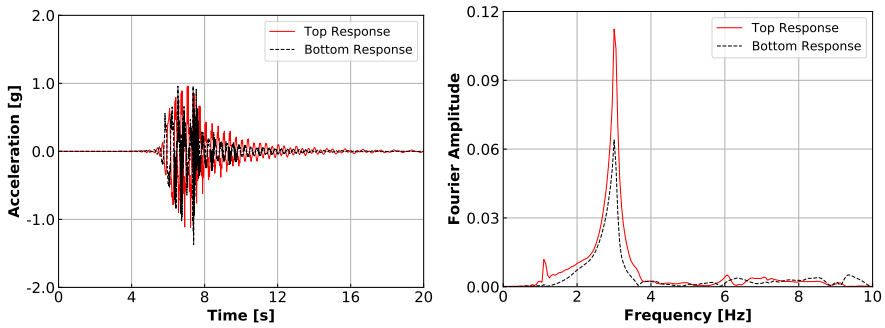

(a) Time history **(b)** FFT Spectrum

Fig. 17. Horizontal acceleration response at top and bottom of the structure when Rayleigh damping ratios ξ for frame and soil are reduced to 0.4% and 1%, respectively.

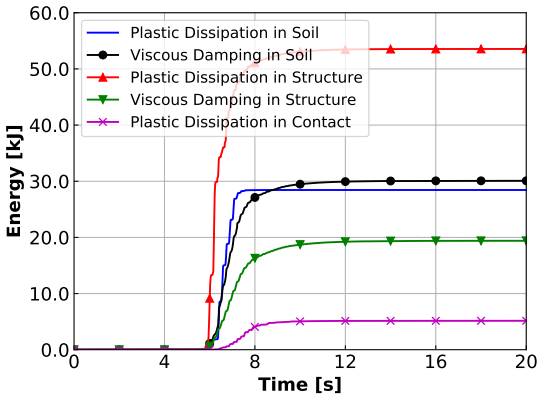

Fig. 18. Total energy dissipation due to different mechanisms in various parts of the SSI model when Rayleigh damping ratio is reduced.

Since plastic dissipation in structure leads to material damage, it is important to choose Rayleigh damping parameters carefully in order to obtain proper information state of the structure after seismic event.

3.4. Influence of Input Ground Motion

The influence of input ground motion on SSI system response and energy analysis is investigated in this section. Figure 19 shows the displacement responses of the frame due to different scaling of input motion. As expected, the peak displacements at the top and bottom decrease when scaled down motions are used. The relationship between the magnitude of input motion and the displacement response of the frame is nonlinear, as expected. In difference from full, benchmark case response that featured significant permanent deformation at the frame bottom, scaled down motions do not produce permanent deformation, as shown in Figure 19 (b).

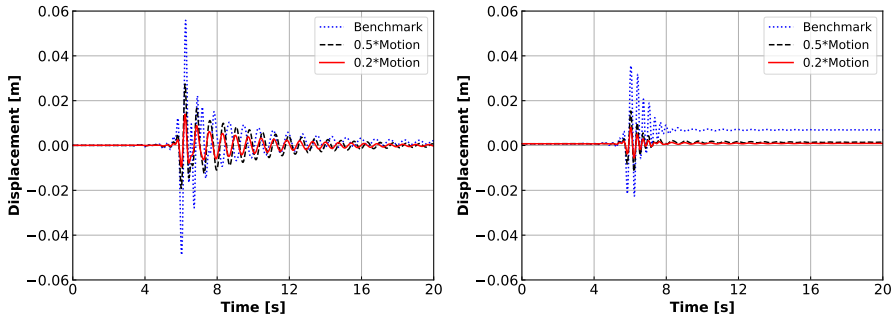

(a) Top Response **(b)** Bottom Response

Fig. 19. Horizontal displacement response using benchmark and scaled down input motions.

Figure 20 shows the maximum IDR results for different scaling of input motion. The maximum IDR response shows more nonlinearity of the SSI system, especially

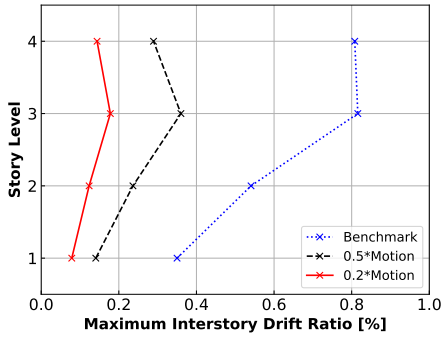

Fig. 20. Maximum IDR results for different scaling of input motion.

for higher floor levels. It is interesting to note that the distribution of maximum IDR along story level changes when the input motion is scaled. For the benchmark case, the maximum IDRs at the third and fourth stories are very close. On the other hand, for the case with 50% scaled input motion, the max IDR at the third floor is clearly larger than that of the fourth floor.

Figure 21 shows the evolution of plastic dissipation density at three locations, frame location C, soil location G, and interface location K, for three different input motion scaling. At all three locations, in frame (C), soil (G), and contact/interface (K), plastic dissipation density increases considerably, nonlinearly when the input motions are scaled up. Quantitatively, taking frame location C as an example, the plastic dissipation density increases more than 10 times when the input motion is doubled. At interface location K, there is no dissipation accumulated at all when the motion scale is equal to or less than 50% of that in the benchmark case. This points out to no frictional slipping between foundation and soil for the two smaller input motions.

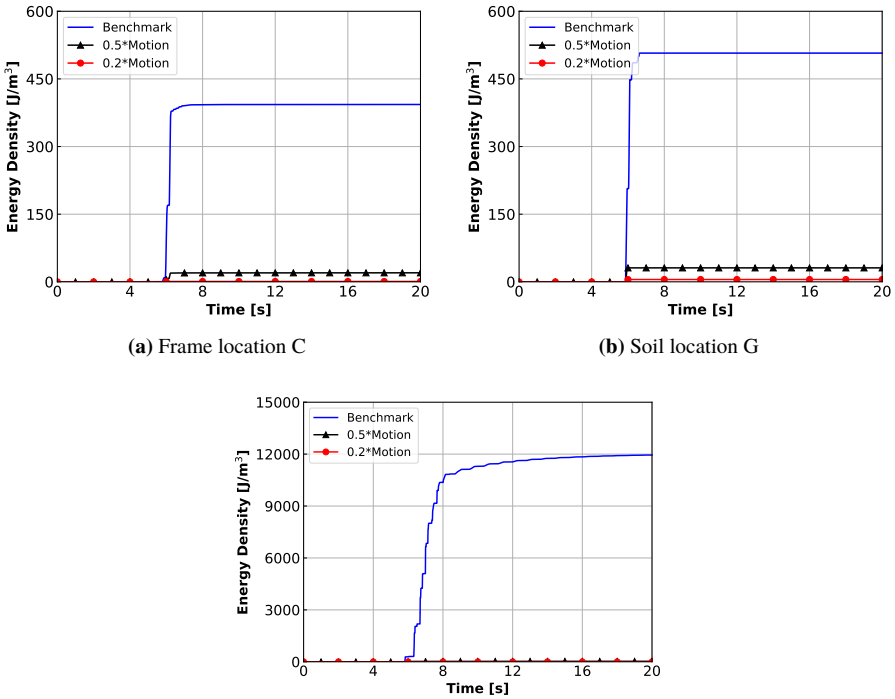

(a) Frame location C

(b) Soil location G

(c) Interface location K

Fig. 21. Evolution of plastic dissipation density for different input motion scaling.

Comparing Figure 19, Figure 20, and Figure 21, it is shown that energy dissipation is more sensitive to the change in input motion magnitude than peak displacement or maximum IDR. For the SSI example analyzed in this study, if displacement or IDR is used as the design parameter to evaluate damage or collapse risk, one may draw the conclusion that the frame structure suffers 2 or 3 times more damage when the seismic motion entering the system becomes twice as large. However, according to the energy dissipation analysis, the actual structural damage could be 10 times more severe.

3.5. Influence of Foundation Type

It is common to have multiple preliminary designs for an engineering project, and then choose the best one by comparing their performances. One possible design change for SSI system is the change in the type of foundation. In this section, the influence of foundation type on SSI performance is analyzed. As seen in Figure 4, the benchmark case has separate, spread foundation underneath each column. For comparison, a case with continuous, slab foundation is analyzed as well.

Figures 22 and 23 show the displacement responses and maximum IDR results of the frame with different foundation designs. The displacement responses and IDR results show differences between the two foundation types. The peak horizontal displacement

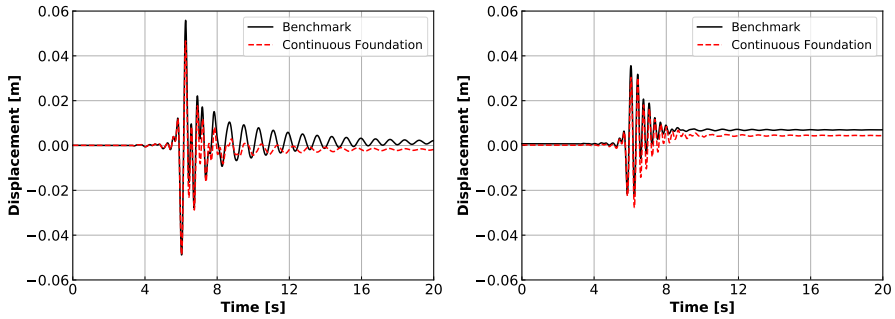

(a) Top Response **(b)** Bottom Response

Fig. 22. Horizontal displacement responses for different foundation types.

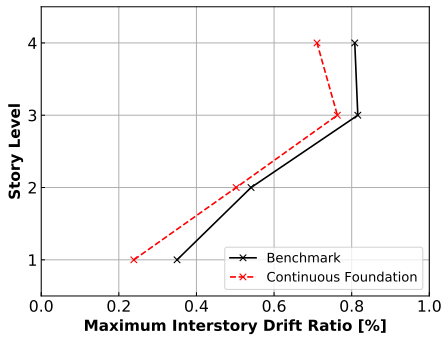

Fig. 23. Maximum IDR results for different foundation types.

and maximum IDR of the third story, that has the largest IDR, reduce less than 10% when the foundation design is changed from spread to continuous, slab foundation. It appears that, according to this result, the change of foundation type does not have significant influence on structural performance for this SSI model.

Figure 24 shows the distribution of plastic energy dissipation for the two cases with different foundation types. Visible differences in plastic dissipation density can be observed in the frame, soil, and interface elements. For continuous, slab foundation, more energy is dissipated in the soil and soil-foundation interface before reaching the structure. This means that less dissipation, or material damage, is accumulated within the frame elements, as can be observed in Figure 24. Please note that the same scale is used for energy dissipation density color in both figures, in order to visually compare dissipation. For example, for a spread foundation case, Figure 24(a), more dissipation is observed in columns on third and fourth floor, in comparison with slab, continuous foundation case, as seen in Figure 24(b).

For quantitative analysis, evolutions of plastic dissipation density at frame location C, soil location G, and interface location K, (see Figure 13 for locations), is presented in Figure 25. At location G, in the soil, there is almost 3 times more energy dissipation

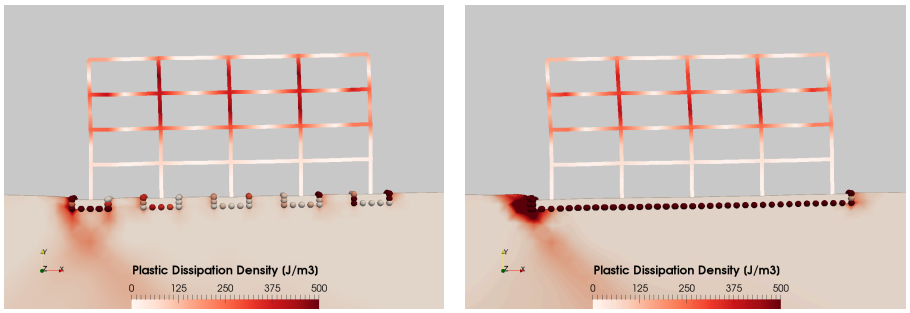

(a) Separate foundations (Benchmark) **(b)** Continuous foundation

Fig. 24. Distribution of plastic energy dissipation for different foundation types.

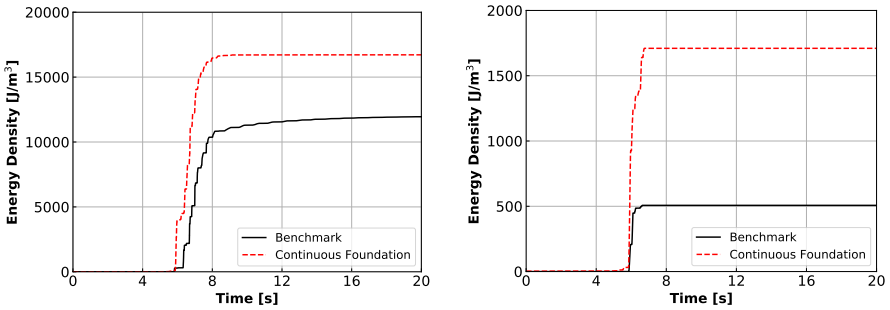

(a) Interface location K **(b)** Soil location G

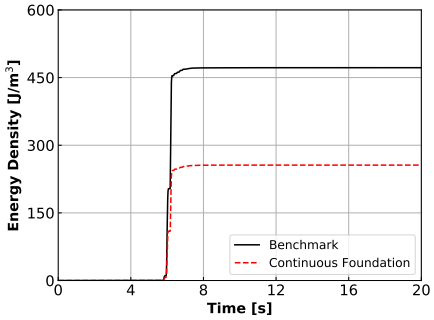

(c) Frame location C

Fig. 25. Evolution of plastic dissipation density at locations: soil K; interface G; and structure C, for different foundation types, benchmark/spread and continuous/slab foundation.

accumulated at the end when a continuous, slab foundation design is used, as opposed to spread foundation. At interface location K, the increase of plastic energy dissipation is approximately 40% with a change from spread to slab foundation type. More

importantly, at location C, in frame, energy dissipation is reduced by 50% when slab foundation design is used as opposed to the spread foundation.

By comparing traditional design parameters, such as peak displacement or maximum IDR, with energy analysis results, it is clear that the former tends to underestimate the variation in system performance when evaluating design changes. This is especially true if seismic performance is the main concern. The source of such underestimation can be largely attributed to the fact that traditional, displacement-based design concepts focus on peak response, while EBD follows accumulated material damage and system performance as a time history throughout the entire loading event.

4. Conclusions

Presented was an energy-based design (EBD) framework for SSI system that was developed based on thermodynamics and engineering mechanics based energy analysis for soil, interfaces and structural components. Traditional force-based and displacement-based design concepts mainly focus on peak response rather than loading history. Thus, for cyclic loads, seismic loads for example, traditional analysis methods cannot account for the continuous accumulation of material damage. On the other hand, energy dissipation can be directly related to damage, hence it is more effective as a design parameter. Existing EBD approaches usually simplify realistic SSI system to simple multiple degree of freedom (MDOF), or even single degree of freedom (SDOF), models. The proposed EBD framework makes use of advanced modeling and simulation techniques with accurate energy dissipation calculations. Such advanced modeling and simulation techniques, together with energy analysis, can provide more accurate and detailed information regarding system performance and safety.

A full earthquake soil structure interaction (ESSI) modeling and simulation that properly models all the components, including earthquake, soil, structure, and soil-foundation interface elements is available and should be used to improve safety and economy of infrastructure objects. The theoretical formulation and computational procedure for calculating energy dissipation in various practical soil and structural material models and finite elements were developed based on the first and second laws of thermodynamics. Presented in this paper was a summary of key theories and formulations that were presented in a series of previous publications [54, 57, 55, 56].

The presented EBD analysis approach is implemented and available within the Real-ESSI Simulator [25] for FE modeling and simulation. Visualization of energy computation results is available within ParaView [6], by using pvESSI plugin, as described in the Real-ESSI documentation `http://real-essi.us/`. Using above numerical tools, the proposed EBD framework can be effectively used for realistic ESSI system modeling with a number of different soil structure systems, The spatial distribution of energy dissipation density, that evolves in time, can be directly analyzed, visualized and used in design and assessment of infrastructure objects.

In order to illustrate the EBD framework, a practical SSI model composed of a frame structure, underlying soil, and soil-foundation interface was analyzed. Material model parameters were calibrated to represent realistic soil and structural materials. An Ormsby wavelet motion was applied to the model using wave potential function and DRM [48, 22, 9, 52]. Full elastic-plastic response of soil, interfaces, and structural

elements was modeled in order to account for displacement proportional, plastic energy dissipation. Rayleigh damping was used to model viscous, velocity proportional damping, energy dissipation in analyzed SSI system.

Traditional design parameters such as displacement and IDR for the benchmark, spread foundation case were briefly discussed. Distribution of time evolving plastic energy dissipation was presented in detail. Spatial locations with high accumulated plastic dissipation were identified in frame, soil, and soil-foundation interface. In addition that, time histories of plastic dissipation density at various locations were used to analyze the ESSI system and to make recommendations for alternative design.

Interesting observations on ESSI response were made based on comparing differently scaled seismic motions and foundation type variations. It was shown that when the input motions were scaled up two times, the peak displacement and maximum IDR of the frame increased 2 to 3 times, while the plastic energy dissipation density at a frame location increased more than 10 times. Similarly, when the foundation type was changed from spread to slab foundation, the peak displacement and maximum IDR decreased less than 10%, however the plastic energy dissipation density at locations within structure was reduced by 50%. These observations indicate that displacement-based design parameters might underestimate the change in ESSI system performance when used to evaluate the influence of input motion scaling or design variation. It was also illustrated how the proposed EBD framework be used in improving safety and economy of infrastructure objects.

5. Acknowledgments

This work was supported in part by the United States Department of Energy (US-DOE), by the Applied Technology Council (ATC) and by the University of California.

References

[1] J. A. Abell, S. K. Sinha, and B. Jeremić. Wavelet based synthetic earthquake sources for path and soil structure interaction modeling: Stress testing of nuclear power plants. In Y. Fukushima and L. Dalguer, editors, *Best Practices in Physics-based Fault Rupture Models for Seismic Hazard Assessment of Nuclear Installations*. IAEA, 2015.

[2] J. A. Abell, N. Orbović, D. B. McCallen, and B. Jeremić. Earthquake soil structure interaction of nuclear power plants, differences in response to 3-D, 3×1-D, and 1-D excitations. *Earthquake Engineering and Structural Dynamics*, 47(6):1478–1495, May 2018. doi: 10.1002/eqe.3026. URL https://onlinelibrary.wiley.com/doi/abs/10.1002/eqe.3026.

[3] K. Aki and P. G. Richards. *Quantitative Seismology*. University Science Books, 2nd edition, 2002.

[4] J. Argyris and H.-P. Mlejnek. *Dynamics of Structures*. North Holland in USA Elsevier, 1991.

[5] P. Armstrong and C. Frederick. A mathematical representation of the multiaxial Bauschinger effect. Technical Report RD/B/N/ 731,, C.E.G.B., 1966.

[6] U. Ayachit. *The ParaView Guide: A Parallel Visualization Application*. Kitware, Inc., USA, 2015. ISBN 1930934300, 9781930934306.

[7] J. P. Bardet and W. Choucair. A linearized integration technique for incremental constitutive equations. *International Journal for Numerical and Analytical Methods in Geomechanics*, 15(1):1–19, 1991.

[8] K.-J. Bathe. Conserving energy and momentum in nonlinear dynamics: a simple implicit time integration scheme. *Computers & Structures*, 85(7):437–445, 2007.

[9] J. Bielak, K. Loukakis, Y. Hisada, and C. Yoshimura. Domain reduction method for three–dimensional earthquake modeling in localized regions. part I: Theory. *Bulletin of the Seismological Society of America*, 93(2):817–824, 2003.

[10] E. Bojórquez, A. Reyes-Salazar, A. Terán-Gilmore, and S. Ruiz. Energy-based damage index for steel structures. *Steel and Composite Structures*, 10(4):331–348, 2010.

[11] T. Caughey. Classical normal modes in damped linear systems. *ASME Journal of Applied Mechanics*, 27:269–271, 1960.

[12] J. Ching, G.-H. Lin, J.-R. Chen, and K.-K. Phoon. Transformation models for effective friction angle and relative density calibrated based on generic database of coarse-grained soils. *Canadian Geotechnical Journal*, 54(4):481–501, 2016.

[13] J. Chung and G. Hulbert. A time integration algorithm for structural dynamics with improved numerical dissipation: the generalized-α method. *Journal of Applied Mechanics*, 60(2):371–375, 1993.

[14] I. Collins and P. Kelly. A thermomechanical analysis of a family of soil models. *Geotechnique*, 52(7):507–518, 2002.

[15] I. F. Collins and G. T. Houlsby. Application of thermomechanical principles to the modelling of geotechnical materials. *Procedings of Royal Society London*, 453: 1975–2001, 1997.

[16] W. Farren and G. Taylor. The heat developed during plastic extension of metals. *Proceedings of the royal society of London A: mathematical, physical and engineering sciences*, 107(743):422–451, 1925.

[17] H. P. Feigenbaum and Y. F. Dafalias. Directional distortional hardening in metal plasticity within thermodynamics. *International Journal of Solids and Structures*, 44(22-23):7526–7542, 2007.

[18] F. C. Filippou, V. V. Bertero, and E. P. Popov. Effects of bond deterioration on hysteretic behavior of reinforced concrete joints. Technical report, Earthquake Engineering Research Center, University of California, Berkeley, 1983.

[19] O. Gonzalez. Exact energy and momentum conserving algorithms for general models in nonlinear elasticity. *Computer Methods in Applied Mechanics and Engineering*, 190(13-14):1763–1783, 2000.

[20] J. F. Hall. Problems encountered from the use (or misuse) of Rayleigh damping. *Earthquake Engineering & Structural Dynamics*, 35(5):525–545, 2006.

[21] C. B. Haselton, C. A. Goulet, J. Mitrani-Reiser, J. L. Beck, G. G. Deierlein, K. A. Porter, J. P. Stewart, and E. Taciroglu. An assessment to benchmark the seismic performance of a code-conforming reinforced-concrete moment-frame building. Technical Report 2007/1, Pacific Earthquake Engineering Research Center, 2008.

[22] N. A. Haskell. The dispersion of surface waves on multilayered media. *Bulletin of the Seismological Society of America*, 43(1):17–34, 1953.

[23] H. M. Hilber, T. J. R. Hughes, and R. L. Taylor. Improved numerical dissipation for time integration algorithms in structural dynamics. *Earthquake Engineering and Structure Dynamics*, 5(3):283–292, 1977.

[24] T. Hughes. *The Finite Element Method ; Linear Static and Dynamic Finite Element Analysis*. Prentice Hall Inc., 1987.

[25] B. Jeremić, G. Jie, Z. Cheng, N. Tafazzoli, P. Tasiopoulou, F. Pisanò, J. A. Abell, K. Watanabe, Y. Feng, S. K. Sinha, F. Behbehani, H. Yang, and H. Wang. *The Real-ESSI Simulator System*. University of California, Davis, 1988-2022. http://real-essi.us/.

[26] B. Jeremić, G. Jie, M. Preisig, and N. Tafazzoli. Time domain simulation of soil–foundation–structure interaction in non–uniform soils. *Earthquake Engineering and Structural Dynamics*, 38(5):699–718, 2009.

[27] D. Kent and R. Park. Flexural members with confined concrete. *ASCE Journal of Structural Division*, 97:1969–1990, 1971.

[28] S. Krenk. Global format for energy-momentum based time integration in nonlinear dynamics. *International Journal for Numerical Methods in Engineering*, 100 (6):458–476, 2014. ISSN 1097-0207. doi: 10.1002/nme.4745. URL http://dx.doi.org/10.1002/nme.4745.

[29] K. L. Lee and H. B. Seed. Drained strength characteristics of sands. *Journal of Soil Mechanics & Foundations Div*, 1967.

[30] P. Léger and S. Dussault. Seismic-energy dissipation in mdof structures. *Journal of Structural Engineering*, 118(5):1251–1269, 1992.

[31] G. Manfredi. Evaluation of seismic energy demand. *Earthquake Engineering & Structural Dynamics*, 30(4):485–499, 2001.

[32] M. Menegotto and P. E. Pinto. Method of analysis for cyclically loaded reinforced clncrete plane frames including changes in geometry and non-elastic behaviour of elements under combined normal force and bending. In *Proceedings of IABSE Symposium*, pages 15–22, 1973.

[33] M. G. Mezgebo and E. M. Lui. A new methodology for energy-based seismic design of steel moment frames. *Earthquake Engineering and Engineering Vibration*, 16(1):131–152, 2017.

[34] A. Moustafa. Damage-based design earthquake loads for single-degree-of-freedom inelastic structures. *Journal of Structural Engineering*, 137(3):456–467, 2011.

[35] N. M. Newmark. A method of computation for structural dynamics. *ASCE Journal of the Engineering Mechanics Division*, 85:67–94, July 1959.

[36] G. Papazafeiropoulos, V. Plevris, and M. Papadrakakis. A new energy-based structural design optimization concept under seismic actions. *Frontiers in Built Environment*, 3:44, 2017.

[37] D. Rittel. An investigation of the heat generated during cyclic loading of two glassy polymers. part i: Experimental. *Mechanics of Materials*, 32(3):131–147, 2000.

[38] P. Rosakis, A. Rosakis, G. Ravichandran, and J. Hodowany. A thermodynamic internal variable model for the partition of plastic work into heat and stored energy in metals. *Journal of the Mechanics and Physics of Solids*, 48(3):581–607, 2000.

[39] H. Ryan. Ricker, Ormsby, Klander, Butterworth - a choice of wavelets. *Canadian Society of Exploration Geophysicists Recorder*, 19(7):8–9, September 1994. URL http://www.cseg.ca/publications/recorder/1994/09sep/sep94-choice-of-wavelets.pdf.

[40] B. Scott, R. Park, and M. Priestley. Fiber element modeling for seismic performance of bridge columns made of concrete-filled frp tubes. *Journal of the American Concrete Institute*, 79(1):13–27, 1982.

[41] J. C. Simo and K. K. Wong. Unconditionally stable algorithms for rigid body dynamics that exactly preserve energy and momentum. *International Journal for Numerical Methods in Engineering*, 31(1):19–52, 1991.

[42] S. K. Sinha and B. Jeremić. Modeling of dry and saturated soil-foundation contact. Technical Report UCD–CompGeoMech–01–2017, University of California, Davis, August 2017.

[43] E. Spacone, F. Filippou, and F. Taucer. Fibre beam–column model for non–linear analysis of r/c frames 1. formulation. *Earthquake Engineering and Structural Dynamics*, 25:711–725, 1996.

[44] E. Spacone, F. C. Filippou, and F. F. Taucer. Fibre beam-column model for non-linear analysis of r/c frames: Part i. formulation. *Earthquake Engineering & Structural Dynamics*, 25(7):711–725, July 1996.

[45] H. Sucuoğlu and A. Nurtuğ. Earthquake ground motion characteristics and seismic energy dissipation. *Earthquake Engineering & Structural Dynamics*, 24(9):1195–1213, 1995.

[46] M. Taiebat and Y. F. Dafalias. SANISAND: Simple anisotropic sand plasticity model. *International Journal for Numerical and Analytical Methods in Geomechanics*, 2008. (in print, available in earlyview).

[47] G. I. Taylor and H. Quinney. The latent energy remaining in a metal after cold working. *Proceedings of the Royal Society of London. Series A, Containing Papers of a Mathematical and Physical Character*, 143(849):307–326, 1934.

[48] W. T. Thomson. Transmission of elastic waves through a stratified solid medium. *Journal of Applied Physics*, 21(2):89–93, 1950.

[49] M. D. Trifunac, T. Ying Hao, and M. I. Todorovska. Energy of earthquake as a design tool. In *Proceedings of 13th Mexican Conference on Earthquake Engineering, XIII MCEE*, pages 1–49, Guadalajara, Mexico, 31th October – 3rd November 2001.

[50] C.-M. Uang and V. V. Bertero. Evaluation of seismic energy in structures. *Earthquake Engineering & Structural Dynamics*, 19(1):77–90, 1990.

[51] E. Veveakis, J. Sulem, and I. Stefanou. Modeling of fault gouges with Cosserat continuum mechanics: Influence of thermal pressurization and chemical decomposition as coseismic weakening mechanisms. *Journal of Structural Geology*, 38: 254–264, 2012.

[52] F. Wang and K. Sett. Time domain stochastic finite element simulation towards probabilistic seismic soil-structure interaction analysis. *Soil Dynamics and Earthquake Engineering*, 116:460 – 475, 2019. ISSN 0267-7261. doi: https://doi.org/10.1016/j.soildyn.2018.10.021. URL http://www.sciencedirect.com/science/article/pii/S0267726118306365.

[53] H. Wang, H. Yang, Y. Feng, F. Wang, and B. Jeremić. Wave potential-domain reduction method for 3D earthquake soil structure interaction. *Soil Dynamics and Earthquake Engineering*, 2020. In review.

[54] H. Yang, S. K. Sinha, Y. Feng, D. B. McCallen, and B. Jeremić. Energy dissipation analysis of elastic-plastic materials. *Computer Methods in Applied Mechanics and Engineering*, 331:309–326, 2018.

[55] H. Yang, Y. Feng, H. Wang, and B. Jeremić. Energy dissipation analysis for inelastic reinforced concrete and steel beam-columns. *Engineering Structures*, 197:109431, 2019. ISSN 0141-0296. doi: https://doi.org/10.1016/j.engstruct.2019.109431. URL http://www.sciencedirect.com/science/article/pii/S0141029618323459.

[56] H. Yang, H. Wang, Y. Feng, and B. Jeremić. Plastic energy dissipation in pressure-dependent materials. *ASCE Journal of Engineering Mechanics*, 2019. In Print.

[57] H. Yang, H. Wang, Y. Feng, F. Wang, and B. Jeremić. Energy dissipation in solids due to material inelasticity, viscous coupling, and algorithmic damping. *ASCE Journal of Engineering Mechanics*, 145(9), 2019.

[58] M. H. M. Yassin. *Nonlinear analysis of prestressed concrete sructures under monotonic and cyclic loads*. PhD thesis, University of California, Berkeley, 1994.

[59] T. F. Zahrah and W. J. Hall. Seismic energy absorption in simple structures. Technical report, University of Illinois Engineering Experiment Station, 1982.

[60] T. F. Zahrah and W. J. Hall. Earthquake energy absorption in sdof structures. *Journal of Structural Engineering*, 110(8):1757–1772, 1984.

[61] H. Ziegler and C. Wehrli. The derivation of constitutive relations from the free energy and the dissipation function. *Advances in Applied Mechanics*, 25:183–238, 1987.